

# Redox-Active Crystalline Coordination Catalyst for Hybrid Electrocatalytic Methanol Oxidation and CO<sub>2</sub> Reduction

Sheng-Nan Sun, Long-Zhang Dong, Jia-Ru Li, Jing-Wen Shi, Jiang Liu,\* Yi-Rong Wang, Qing Huang, and Ya-Qian Lan\*

**Abstract:** Hybrid CO<sub>2</sub> electroreduction (HCER) is recognized as an important strategy to improve the total value of redox products and energy conversion efficiency. In this work, a coordination catalyst model system (Ni<sub>8</sub>-TET with active oxidation sites, Ni-TPP with active reduction sites and PCN-601 with redox-active sites) for HCER was established for the first time. Especially, PCN-601 can complete both anodic methanol oxidation and cathodic CO<sub>2</sub> reduction with FE<sub>HCOOH</sub> and FE<sub>CO</sub> over 90%. The performance can be further improved with light irradiation (FE nearly 100%). DFT calculations reveal that the transfer of electrons from Ni<sup>II</sup><sub>8</sub> clusters to metalloporphyrins under electric fields results in the raised oxidizability of Ni<sub>8</sub> clusters and the raised reducibility of metalloporphyrin, which then improves the electrocatalytic performance. This work serves as a well-defined model system and puts forward a new design idea for establishing efficient catalysts for hybrid CO<sub>2</sub> electroreduction.

Therefore, the best way to improve the energy utilization efficiency of the whole electrolyzer is to find a thermodynamically more favorable anodic oxidation reaction to replace OER, and to couple it with CO<sub>2</sub>RR for the co-production of high-value chemicals, for example, a hybrid CO<sub>2</sub> electroreduction (HCER) containing methanol oxidation (MOR) coupled with CO<sub>2</sub>RR.<sup>[5]</sup> In this way, not only more valuable products can be obtained at the anode, but also the overall electrocatalytic reaction rate and energy conversion efficiency can be improved.<sup>[6]</sup> Currently, some nanomaterial catalysts have been reported for HCER (such as MOR coupled with CO<sub>2</sub>RR). However, in most catalytic systems, two different types catalysts are required to be designed for anodic MOR and cathodic CO<sub>2</sub>RR, respectively.<sup>[7]</sup> From a practical application point of view, in this hybrid electrocatalytic full reaction system, it is more desirable to use one catalyst for both MOR and CO<sub>2</sub>RR to reduce catalytic cost and simplify electrolysis devices. Moreover, the structures of these reported nanomaterial catalysts are multi-phase composites with complicated interfacial information, from which it is difficult to obtain a clear understanding of the relationship between the structure and the performance of the catalysts. It would be more advisable to design and construct a bifunctional catalyst with a well-defined structure to be used as both anode and cathode in HCER systems.

Theoretically, to achieve the expectation that one catalyst can be used to realize the anodic MOR and cathodic CO<sub>2</sub>RR simultaneously, an excellent strategy is to assemble the active sites for MOR and the active sites for CO<sub>2</sub>RR into the structure of one catalyst. Moreover, if electrons can be transferred from the oxidation active sites to the reduction active sites under the action of an electric field, this will lead to a higher valence state in the part where the oxidation reaction occurs and a lower valence state in the part where the reduction reaction occurs. Thus, during the process of HCER, it will be more active in both oxidation and reduction reactions, and the energy use efficiency of the whole electrolyzer will be further improved. Based on this design concept, we believe that well-structured crystalline coordination catalysts can offer more opportunities for the realization of this idea. It is well known that coordination compounds are crystalline materials bridged by metal ions/clusters and organic ligands periodically. If these crystalline materials are used as catalysts, their structures can be adjusted or designed according to specific requirements. Besides, their well-defined structural information is very beneficial for the mechanistic studies of catalytic reactions.<sup>[8]</sup>

## Introduction

Electrocatalytic anodic organic oxidation reaction coupled with carbon dioxide reduction reaction (CO<sub>2</sub>RR) presents an obvious advantage in improving the total value of redox products and overall energy conversion efficiency of the hybrid electrocatalytic full reaction.<sup>[1]</sup> In conventional electrocatalytic CO<sub>2</sub> reduction electrolyzers, the CO<sub>2</sub>RR and the oxygen evolution reaction (OER) occur at cathode and anode, respectively.<sup>[2]</sup> However, the OER with slow kinetics not only consumes a large amount of energy ( $\approx 90\%$  of the total power input) but also largely limits the generation of cathodic products from CO<sub>2</sub>RR, hindering the conversion efficiency of CO<sub>2</sub>RR.<sup>[1d,3]</sup> In addition, although oxygen as the product of OER is eco-friendly, it is usually released directly into the environment due to its low economic value, which indirectly leads to the loss of energy conversion.<sup>[4]</sup>

[\*] S.-N. Sun, L.-Z. Dong, J.-R. Li, J.-W. Shi, Prof. J. Liu, Y.-R. Wang, Q. Huang, Prof. Y.-Q. Lan  
 School of Chemistry, South China Normal University  
 Guangzhou, 510006 (China)  
 E-mail: liuj0828@m.scnu.edu.cn  
 yqlan@njnu.edu.cn  
 yqlan@m.scnu.edu.cn

However, due to the high requirements for structural stability in electrocatalytic reactions, only a very small number of crystalline coordination compounds can be used as electrocatalysts. Among these catalysts, crystalline coordination catalysts that can be used for HCER have not been reported yet. Particularly, using one bifunctional crystalline coordination catalyst for both anodic and cathodic reactions is fairly challenging.

In this system, three crystalline coordination compounds (Ni-TPP, Ni<sub>8</sub>-TET and PCN-601) electrocatalysts were constructed for MOR, CO<sub>2</sub>RR and HCER (MOR coupled with CO<sub>2</sub>RR), respectively. When Ni-TPP and Ni<sub>8</sub>-TET were used as electrocatalysts for CO<sub>2</sub>RR and MOR respectively, the Ni in the center of porphyrins as the reduction active sites can reduce CO<sub>2</sub> to CO with a Faraday efficiency (FE<sub>CO</sub>) of 25.6% and the Ni<sub>8</sub><sup>II</sup> clusters as the oxidation active sites can oxidize methanol to formic acid (HCOOH) with a Faraday efficiency (FE<sub>HCOOH</sub>) of 86.3%. It is worth noting that when PCN-601 assembled with a Ni<sub>8</sub> cluster and metalloporphyrin (Ni) was used as an electrode material, the MOR and CO<sub>2</sub>RR performance of PCN-601 (FE<sub>HCOOH</sub> of 89%, FE<sub>CO</sub> of 96%) is stronger than that of Ni<sub>8</sub>-TET (86.3%) and Ni-TPP (25.6%). Besides, this combined bifunctional crystalline catalyst can be used as both anode and cathode for HCER with an FE<sub>HCOOH</sub> over 90% (2.1–2.4 V) and FE<sub>CO</sub> over 80% (1.9–2.5 V). Additionally, by light irradiation, the FE<sub>HCOOH</sub> can be further increased to more than 90% in a wide potential range (1.8–2.5 V) and FE<sub>CO</sub> to nearly 100%. The theoretical calculations demonstrate that the electrons transfer from the Ni<sub>8</sub> clusters to the Ni ions in the center of porphyrins during the catalytic process, which leads to the enhanced oxidizability of the Ni<sub>8</sub> clusters and the enhanced reducibility of the Ni ions in porphyrins and ultimately results in the enhancement of both Faraday efficiencies. This is the first report in which one crystalline coordination catalyst is used to complete both the cathodic and anodic reactions of HCER electroreduction.

## Results and Discussion

Based on our previous work and previously reported literature, the Ni-TPP, Ni<sub>8</sub>(OH<sub>2</sub>)<sub>2</sub>(OH)<sub>4</sub>(tet)<sub>6</sub> (abbreviated as Ni<sub>8</sub>-TET) and PCN-601 were synthesized by a solvothermal method.<sup>[9,10]</sup> The phase purity of the three crystalline coordination compounds was determined by powder X-ray diffraction (PXRD). As displayed in Figures S1–S3, the synthesized samples are in good agreement with the simulated patterns, indicating the successful synthesis and good phase purity of three compounds. The structure details of the resulting PCN-601, Ni<sub>8</sub>-TET and Ni-TPP are shown in Figure 1. The Ni<sub>8</sub>-TET is a three-dimensional (3D) MOF composed of straight-chain ligands (H<sub>2</sub>tet) and pyrazole-NiOx coordination spheres (shortened as Ni<sub>8</sub> cluster) (Figure 1a). The structure of Ni-TPP is shown in Figure 1b, it is composed of a Ni ion and porphyrin ligand (5,10,15,20-Tetraphenyl-21*H*,23*H*-porphine, TPP). For PCN-601, the  $\pi$ -conjugation Ni metalloporphyrin centers connect Ni<sub>8</sub> clus-

ters to generate the 3D porous framework of PCN-601 (Figure 1c). X-ray photoelectron spectroscopy (XPS) was carried out to trace the surface chemical state of metal atoms in these three compounds. As can be seen in Figures S4–S6, the Ni 2p spectrum of the three compounds deconvoluted into two peaks with a binding energy of 855.6 and 873.0 eV corresponding to Ni<sup>2+</sup>.<sup>[11]</sup> Besides, Fourier transform infrared spectroscopy (FTIR) characterization and thermogravimetric analysis (TGA) were also performed. Compared with H<sub>4</sub>TPP and TPP ligands, the disappeared peaks at 3315 cm<sup>-1</sup> and 966 cm<sup>-1</sup> and the new peak at 999 cm<sup>-1</sup> in the FTIR spectrum of PCN-601 and Ni-TPP are assigned to the stretching vibration peak, bending vibration peak of N–H of porphyrin ligand, and the Ni–N stretching vibration peaks of PCN-601 and Ni-TPP, respectively (Figures S7–S9).<sup>[12]</sup> This result indicates that Ni<sup>2+</sup> ions are indeed coordinated with porphyrin ligands. The TGA results show the thermal decomposition temperature (at least 450 °C) of the frameworks of three compounds, indicating their high structure thermostability (Figures S10–S12). Given that chemical stability is very important for crystalline electrocatalysts to evaluate their electrochemical performance, PCN-601, Ni<sub>8</sub>-TET and Ni-TPP were immersed in solutions of different pH for 48 hours to explore their structural rigidity (Figures S13–S15). It is found that the PXRD patterns of immersed compounds are matched well with patterns before treatment, suggesting that no phase transition or skeleton collapse occurred during this process.

Initially, a series of electrochemical measurements were carried out in a three-electrode setup to explore the electrocatalytic performance of Ni<sub>8</sub>-TET and Ni-TPP for MOR and CO<sub>2</sub>RR, respectively. The liquid products can be confirmed by <sup>1</sup>H nuclear magnetic resonance (<sup>1</sup>H-NMR) and ion chromatography (IC) measurement (Figures S16–S18). The gaseous products were detected by gas chromatography (GC) (Figure S19). Compared with the linear sweep voltammetry (LSV) curve of Ni<sub>8</sub>-TET in 1 M KOH without methanol, the LSV curve of Ni<sub>8</sub>-TET in 1 M KOH with 0.1 M methanol shows rapidly increasing current densities, indicating that methanol oxidation is more likely to occur at the anode rather than OER (Figure S20).<sup>[13]</sup> Similarly, the higher current densities of the LSV curve of Ni-TPP in CO<sub>2</sub>-saturated 0.5 M KHCO<sub>3</sub> solution than in Ar-saturated 0.5 M KHCO<sub>3</sub> solution illustrates that CO<sub>2</sub>RR is preferred to the hydrogen evolution reaction (HER) at the cathode (Figure S21). The Faradaic efficiency of the MOR to HCOOH (FE<sub>HCOOH</sub>) and the Faradaic efficiency of the CO<sub>2</sub>RR to carbon monoxide (FE<sub>CO</sub>) can be calculated from the quantitative results of IC and GC, respectively. As shown in Figure 2a, Ni<sub>8</sub>-TET demonstrates a catalytic activity for MOR with a FE<sub>HCOOH</sub> over 50% at a potential range from 1.3 to 1.7 V vs. RHE and reaches a maximum value of 93% at 1.5 V vs. RHE. Besides, the results of the CO<sub>2</sub>RR test show that Ni-TPP has a certain CO<sub>2</sub>RR activity with the highest FE<sub>CO</sub> value of 25% at the potential of –0.9 V vs. RHE (Figure S22) and the <sup>1</sup>H-NMR spectrum shows that no liquid products are discovered (Figure S23). Some comparative experiments were carried out to confirm the sources of

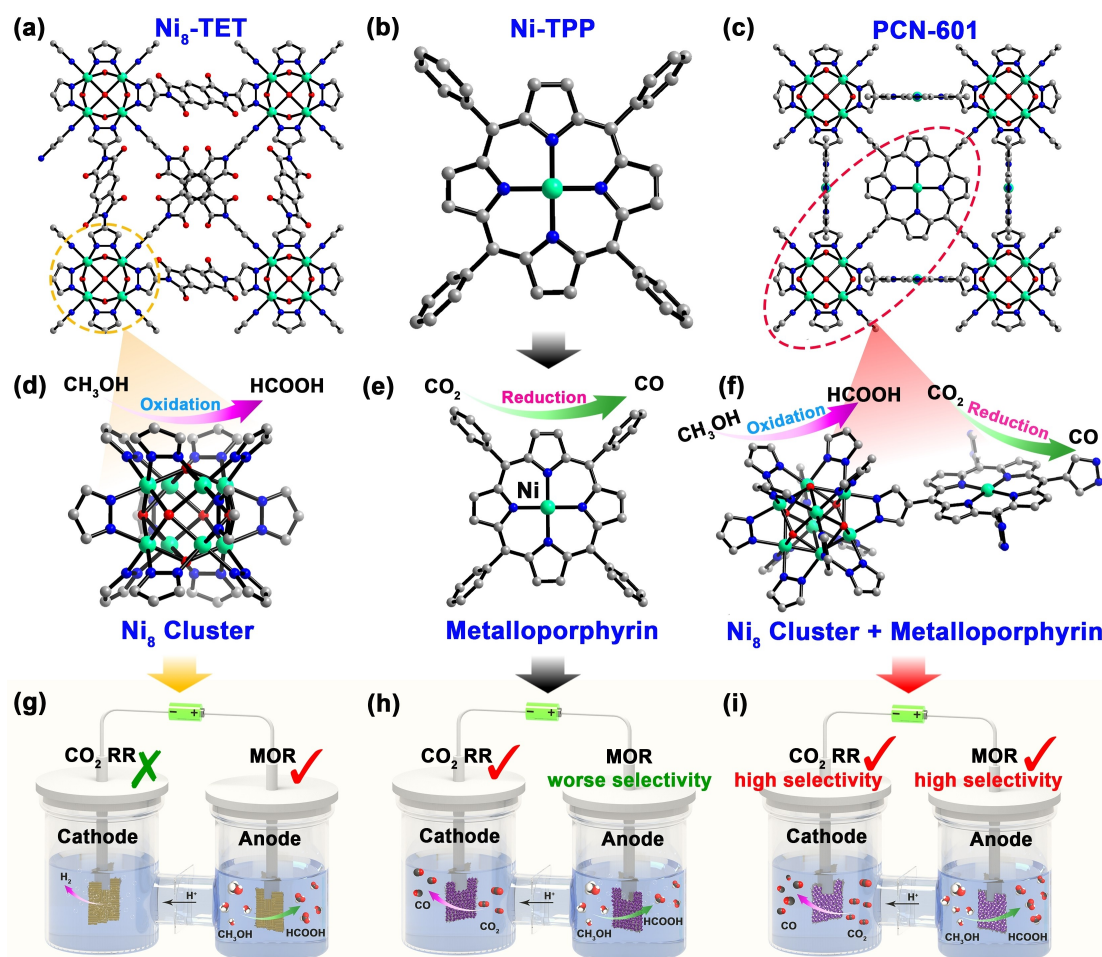


**Figure 1.** a) Structure representation of Ni<sub>8</sub>-TET (3D structure formed by straight-chain ligands connecting with pyrazole-NiOx coordination spheres). b) Structure representation of Ni-TPP (supramolecular structure formed by the accumulation of metalloporphyrin single molecules through hydrogen bonds and  $\pi$ - $\pi$  interactions). c) Structure representation of PCN-601 (3D porous framework formed by metalloporphyrin connecting with pyrazole-NiOx coordination spheres). d–f) Potential catalytically active sites of three crystalline coordination compounds used as catalysts. g–i) Performance speculation of three crystalline coordination catalysts applied in electrolytic cell.

catalytic activity of catalysts. As shown in Figures S24 and S25, carbon paper and other additives (AB and Nafion) do not affect MOR and CO<sub>2</sub>RR activity. Additionally, the MOR activity of H<sub>2</sub>tet and the CO<sub>2</sub>RR activity of TPP were tested, respectively. The corresponding results show that both H<sub>2</sub>tet and TPP have poor catalytic performance as the FE<sub>HCOOH</sub> of H<sub>2</sub>tet for MOR is below 10% at different applied potentials and H<sub>2</sub> is the main product of TPP for CO<sub>2</sub>RR (Figures S26 and S27). The above results indicate that the catalytic active sites of MOR are Ni<sub>8</sub> clusters, and the catalytically active sites of CO<sub>2</sub>RR are Ni ions in the center of porphyrins.

Then, the MOR and CO<sub>2</sub>RR activities of PCN-601 composed of Ni<sub>8</sub> clusters (active sites for MOR) and nickel metalloporphyrins (active sites for CO<sub>2</sub>RR) were evaluated. As expected, PCN-601 has both MOR and CO<sub>2</sub>RR electrocatalytic properties. Figure 2b shows the OER and MOR activity of PCN-601 evaluated by LSV at the anode in 1 M KOH and 1 M KOH with 0.1 M methanol, respectively. The current density of PCN-601 increases markedly in 1 M KOH

solution with 0.1 M methanol, and PCN-601 required a potential of 1.40 V vs. RHE to drive a current density of 10 mA cm<sup>-2</sup> when catalyzing MOR, negatively shifted by 175 mV compared to that of OER (Figure S28). Besides, the reaction kinetics for MOR and OER during the electrochemical process were evaluated by the Tafel plots derived from the LSV results. As can be seen in the insert in Figure 2b, the Tafel slope of MOR is 156.6 mV dec<sup>-1</sup>, which is much lower than that of OER (176.7 mV dec<sup>-1</sup>). These results indicate that MOR is more conducive than OER. Similarly, Figure 2c shows the polarization curves of PCN-601 in CO<sub>2</sub>- or Ar-saturated 0.5 M KHCO<sub>3</sub> solution, which shows a remarkable CO<sub>2</sub>RR performance as a much higher current density in CO<sub>2</sub>-saturated KHCO<sub>3</sub> solution than that in Ar-saturated KHCO<sub>3</sub> solution. Moreover, the activities and Faradaic efficiencies of MOR and CO<sub>2</sub>RR were quantified by controlled potential electrolysis. The results as shown in Figure 2d and e, FE<sub>HCOOH</sub> of PCN-601 is quite high at above 85% in the potential range from 1.4 to 1.6 V vs. RHE, and the FE<sub>CO</sub> of PCN-601 reaches a maximum value

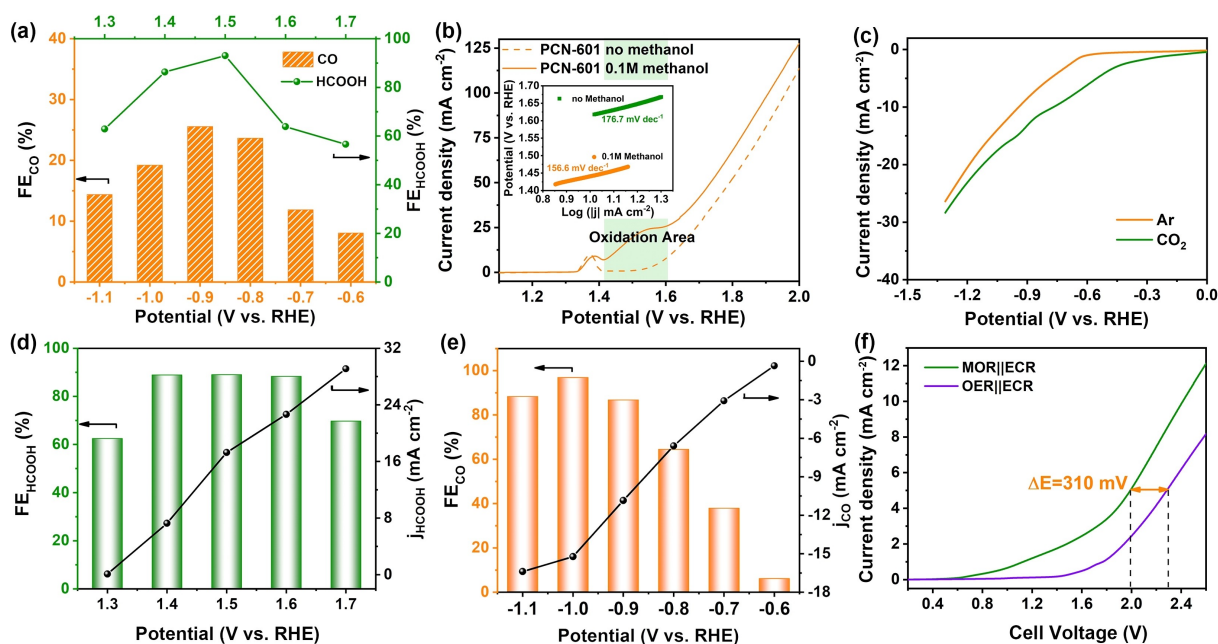


**Figure 2.** Electrochemical performances of Ni<sub>8</sub>-TET, Ni-TPP and PCN-601: a) FE<sub>HCOOH</sub> of Ni<sub>8</sub>-TET for MOR test and FE<sub>CO</sub> of Ni-TPP for CO<sub>2</sub>RR test. b) LSV curves of PCN-601 at anode in 1M KOH with and without the addition of 0.1 M methanol and Tafel plots (insert) for MOR derived from the LSV results. c) Polarization curves of PCN-601 in CO<sub>2</sub>- or Ar- saturated 0.5 M KHCO<sub>3</sub> solution. d) FE<sub>HCOOH</sub> and j<sub>HCOOH</sub> of PCN-601 during MOR test. e) FE<sub>CO</sub> and j<sub>CO</sub> of PCN-601 for CO<sub>2</sub>RR. f) Cell LSV curve comparison of MOR || CO<sub>2</sub>RR and OER || CO<sub>2</sub>RR using PCN-601 as both anode and cathode.

of 97% at  $-1.0$  V vs. RHE, indicating a significantly high activity for the conversion of methanol to HCOOH and CO<sub>2</sub> to CO, respectively. In addition, the partial current density of PCN-601 for MOR and CO<sub>2</sub>RR can reach  $29.1 \text{ mA cm}^{-2}$  and  $-16.4 \text{ mA cm}^{-2}$ , respectively (Figure 2d,e). By comparing the catalytic performance of the three compounds (PCN-601, Ni<sub>8</sub>-TET and Ni-TPP), it can be found that the MOR performance of PCN-601 is better than that of Ni<sub>8</sub>-TET, and the CO<sub>2</sub>RR performance of PCN-601 is far superior to that of Ni-TPP (Figure S29 and S30). Moreover, the results of electrochemical impedance spectroscopy (EIS) measurements show that the shuttle of charge transfer on PCN-601 is faster than that of Ni<sub>8</sub>-TET and Ni-TPP because the semicircle of PCN-601 has the smallest diameter (Figure S31). The reason for the differences in performances may be that in the process of electrocatalysis, the electrons of electron-rich Ni<sub>8</sub> clusters are transferred to the electron-deficient centers of porphyrins, so that the electrocatalytic activities of the redox-active sites in PCN-601 are improved.

Inspired by the excellent electrocatalytic performance of PCN-601 for anodic MOR and cathodic CO<sub>2</sub>RR, a hybrid CO<sub>2</sub> electroreduction electrolyzer combining anodic MOR and cathodic CO<sub>2</sub>RR (denoted as MOR||CO<sub>2</sub>RR), with concurrent high valued products generation, was further pursued to assess the feasibility of its practical application. As shown in Figure 2f, the benefit of MOR in lowering the cell potential was verified by the polarization curves. The pair of MOR||CO<sub>2</sub>RR only needs 1.99 V to deliver a current density of  $5 \text{ mA cm}^{-2}$  for the formation of CO and HCOOH, which is 310 mV lower than that for OER||CO<sub>2</sub>RR.

To ensure the anodic methanol oxidation and the cathodic CO<sub>2</sub> electroreduction retain their excellent electrocatalytic performance, the products from the anode and cathode were separately collected and the FEs were calculated (Figure S32 and S33). In comparison with OER||CO<sub>2</sub>RR cell (FE<sub>CO</sub> < 65%, Figure S32), the CO<sub>2</sub>RR performance was improved in the two-electrode electrolyzer when MOR was coupled to CO<sub>2</sub>RR. The corresponding cathodic CO<sub>2</sub>RR produced CO with increasing Faradaic efficiencies at cell voltage windows from 1.8 to 2.5 V and the Faradaic efficiencies can be maintained at more than 80% in the range of 2.1 to 2.5 V. Besides, the corresponding anodic MOR produced HCOOH with Faradaic efficiencies over 75% at all applied voltages and toward a maximum value of 93% (Figure 3a).

Metalloporphyrins as photosensitive macrocyclic compounds possess efficient light absorption capabilities (Figure S34).<sup>[14]</sup> Moreover, photoelectrocatalysis has been proven as a promising approach for producing high-value chemicals.<sup>[15]</sup> Given these, we proposed that light irradiation probably facilitates electrochemical activation of HCER. To verify this hypothesis, we carried out the electrochemical test of hybrid CO<sub>2</sub> electroreduction with light irradiation (PHCER) in a two-electrode electrolyzer. Before evaluating the electrochemical activity of PHCER, we conducted a photo-current response test of PCN-601 at different applied potentials. Figure 3b shows that the current densities increase obviously with the assistance of light, which provides a good test basis for the next PHCER test. The results of the PHCER test are shown in Figure 3c,d and S35, compared with HCER, the FE<sub>HCOOH</sub> of PHCER is improved

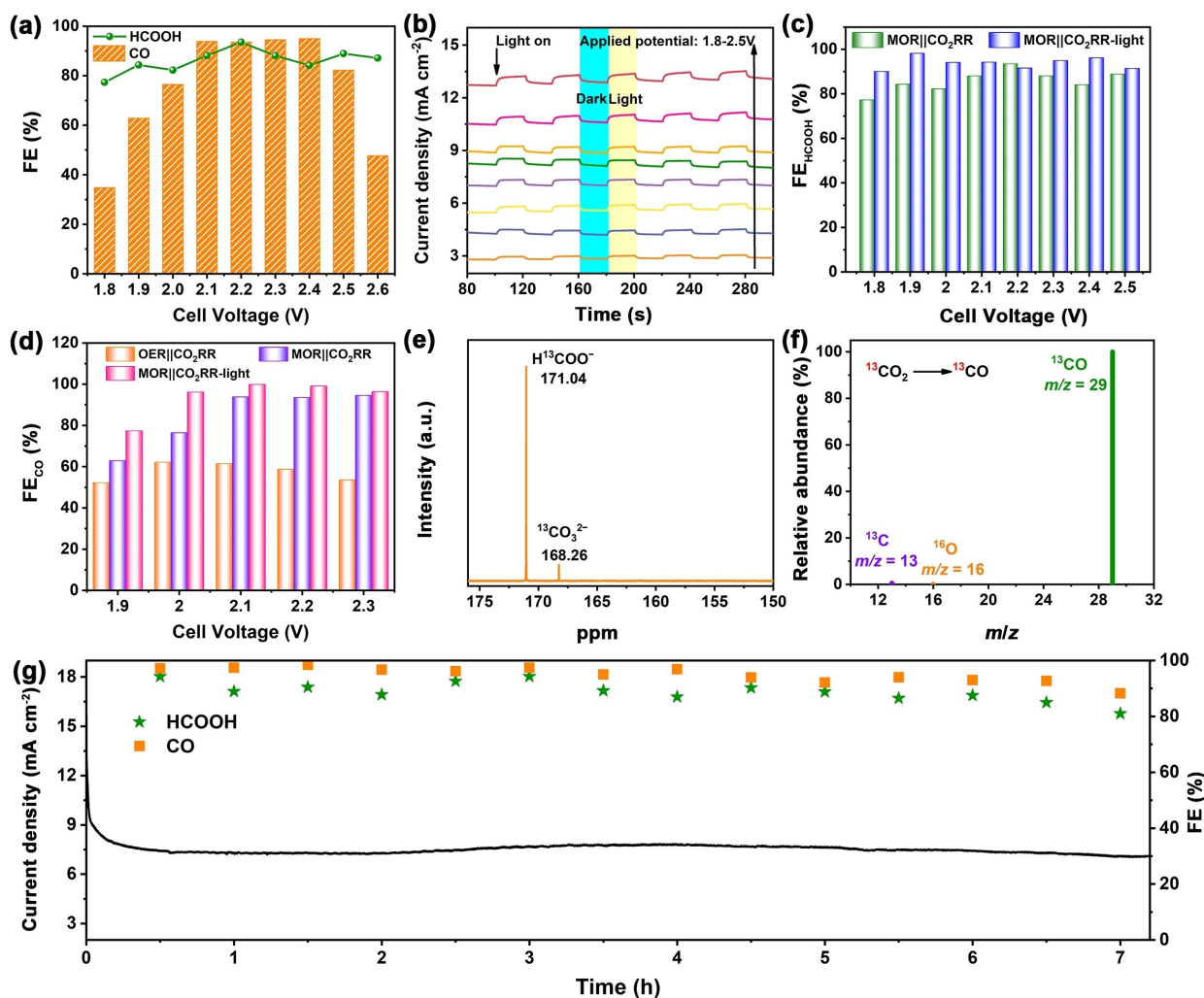


**Figure 3.** Electrochemical performances of PCN-601 for hybrid CO<sub>2</sub> electroreduction: a) The FE<sub>HCOOH</sub> and FE<sub>CO</sub> of MOR || CO<sub>2</sub>RR. b) Photo-current response curves of PCN-601 at different bias voltage. c) FE<sub>HCOOH</sub> of MOR || CO<sub>2</sub>RR and MOR || CO<sub>2</sub>RR with light at different potentials. d) The FE<sub>CO</sub> of MOR || CO<sub>2</sub>RR, OER || CO<sub>2</sub>RR and MOR || CO<sub>2</sub>RR with light at different potentials using PCN-601 as anode and cathode. e) <sup>13</sup>C-NMR spectrum of the electrolyte after MOR electrochemical test. f) The mass spectra of <sup>13</sup>CO recorded under <sup>13</sup>CO<sub>2</sub> atmosphere of gaseous product (CO) for CO<sub>2</sub>RR. g) Stability of PCN-601 for HCER at 2.1 V cell voltage.

to over 90 % in all applied cell voltages from 1.8 to 2.6 V and FE<sub>CO</sub> can be maintained above 95 % in a broad voltages windows (2 to 2.3 V) and even close to 100 % at 2.1 and 2.2 V.

To verify the carbon source of oxidation and reduction products during the process of MOR and CO<sub>2</sub>RR, isotopic experiments were performed by adopting <sup>13</sup>CH<sub>3</sub>OH instead of CH<sub>3</sub>OH in the anodic electrolyte and using <sup>13</sup>CO<sub>2</sub> as a substitute for <sup>12</sup>CO<sub>2</sub> in the cathode. <sup>13</sup>C-NMR spectrum confirms the generation of formate, as shown in Figure 3e, the peaks at about 171.04 ppm and 168.26 ppm correspond to HCOO<sup>-</sup> and CO<sub>3</sub><sup>2-</sup>, respectively. The main products of CO<sub>2</sub>RR were analyzed by gas chromatography/mass spectrometry (Figure 3f), and the result shows that the peaks at *m/z* = 13, 16, 29 are assigned to <sup>13</sup>C, <sup>16</sup>O and <sup>13</sup>CO, respectively. These results fully prove that the products of MOR and CO<sub>2</sub>RR indeed derive from the CH<sub>3</sub>OH and CO<sub>2</sub> used in experiments.

The persistence of the catalytic effect is an important parameter of the catalytic performance of the catalyst. A chronoamperometric test was conducted to unveil the stability of PCN-601 in the electrocatalytic process. As exhibited in Figure 3g, the HCER performance of PCN-601 can be maintained for 7 hours with FE<sub>HCOOH</sub> over 85 % and FE<sub>CO</sub> over 90 %. Besides, the samples after the electrochemical test were collected for the PXRD test. The results show that the diffraction peaks of the samples after the electrochemical test are consistent with that before the test, which showed that the catalyst has excellent electrocatalytic stability (Figure S36).

In situ FTIR measurements were performed to ascertain the intermediates during the MOR and CO<sub>2</sub>RR processes, respectively. For MOR, the bands at 2950 and 2841 cm<sup>-1</sup> in the spectra are ascribed to surface CH<sub>3</sub>OH species. The peak at 1473 cm<sup>-1</sup> can be assigned to CH<sub>2</sub>O\*.<sup>[16]</sup> It can be seen that there are five peaks at 1655, 1565, 1403, 1332 and

1299  $\text{cm}^{-1}$  in the lower wavenumber region which are assigned to the C=O stretch, asymmetric stretch, symmetric stretch, C–O stretch, OH deformation of  $\text{HCOOH}^*$ , respectively (Figure 4a).<sup>[17]</sup> Besides, Figure 4b shows the in situ FTIR spectrum of  $\text{CO}_2\text{RR}$ , in which, the peaks at 1664–1280  $\text{cm}^{-1}$  are ascribed to  $\text{COOH}^*$  (the key intermediate for the formation of CO). And the IR absorption band of chemisorbed  $\text{CO}/\text{CO}^*$  is detected at 2100  $\text{cm}^{-1}$ .<sup>[18]</sup>

Density functional theory (DFT) calculations were conducted to discuss the electrocatalytic mechanism and the cause of the improved activity. Firstly, electric field exerted from different directions was applied to the system to discuss

its effect on PCN-601. It can be found that when an electric field is applied to the system, no matter what direction of it (Figure 5a), the Ni in the center of porphyrin can be relatively negatively charged and the Ni in the  $\text{Ni}_8$  cluster can be relatively positively charged. This means that as long as an electric field is applied to the system, the charge will be transferred from the  $\text{Ni}_8$  cluster to the porphyrin. Then, the reactions were studied by using the computational hydrogen electrode method (CHE method,<sup>[19]</sup> see Supporting Information for calculation details) to calculate the free energy diagram (FED) of  $\text{CO}_2\text{RR}$  and MOR on the  $\text{Ni}_8$  cluster and Ni-TPP, respectively. As shown in Figure 5b–5c, the  $\text{CO}_2\text{RR}$  activity of the  $\text{Ni}_8$  cluster is worse than that of Ni-TPP ( $\Delta G_{\text{max}}^0 = 1.50$  vs. 0.68 eV,  $\Delta G_{\text{max}}^0$  stands for the max standard Gibbs energy among all the elementary steps), while the MOR activity of  $\text{Ni}_8$  cluster is better than that of Ni-TPP ( $\Delta G_{\text{max}}^0 = -0.64$  vs.  $-0.55$  eV), which corresponds to the experimental results.

Additionally, we can also read some extra information from the DFT based results. Firstly, for  $\text{Ni}_8$  cluster, the key intermediates of  $\text{CO}_2\text{RR}$ , the  $\text{COOH}$  and  $\text{CO}$ , are not directly bound with  $\text{Ni}_8$  cluster. They are only physically adsorbed on the surface, which is responsible for the poor  $\text{CO}_2\text{RR}$  activity of  $\text{Ni}_8$  cluster. Secondly, for MOR, both  $\text{Ni}_8$  cluster and Ni-TPP choose to break the C–H bond after generating  $\text{CH}_3\text{OH}^*$ , then the O–H bond is immediately disconnected after the formation of  $\text{H}_2\text{COH}^*$ . Besides, the calculation results show that a side reaction that occurs after the formation of  $\text{CHO}^*$  to generate  $\text{CO}_2$  is less likely to continue because the reaction energy of the side reaction is more positive than that of MOR path (Figure S37–S38).<sup>[17b,20]</sup> Third, the rate-determining step (RDS) on Ni-TPP for  $\text{CO}_2\text{RR}$  is  $\text{CO}_2 + \text{H}_2\text{O} \rightarrow \text{COOH} + \text{OH}^-$ . Further than that, considering Ni porphyrin will receive electrons from  $\text{Ni}_8$  cluster, we add an additional electron to see the result of this behavior. Consequently, we see the reaction energy of this step reduced by 0.26 eV, indicating that charge transfer is favorable for the RDS of  $\text{CO}_2\text{RR}$ . This is one first benefit of  $\text{Ni}_8$  cluster. In fact, the reason why the adsorption of  $\text{COOH}$  on Ni-TPP is affected by charge has been discussed in the previous literature. This is caused by a dipole-electric field interaction: adsorbed  $\text{COOH}$  has a dipole  $\mu$  that points directly to the metal center (from negative center to positive center); accepting electrons will also raise an additional electric field  $E$  that points towards metal center. This will then result in an additional contribution to adsorption energy by  $\Delta E = -E \cdot \mu$ , thus aid the adsorption of  $\text{COOH}$ , resulting in a change in its activity.<sup>[21]</sup>

Another benefit of the  $\text{Ni}_8$  cluster lies in the kinetics of the RDS of  $\text{CO}_2\text{RR}$ . The reaction mentioned in this work mainly takes place at neutral pH, in which water acts as the main proton donor. In this case, the efficiency of proton donation is quite correspondent to the oxophilicity of the catalyst. The higher the oxophilicity of the catalyst, the higher the kinetics.<sup>[22]</sup> For PCN-601 and Ni-TPP, the adjacent groups to porphyrin are different. PCN-601 connects with pyrazole, while Ni-TPP connects with benzene. They may provide different oxophilicity and different activities. To better show this, we should compare the role of these two different

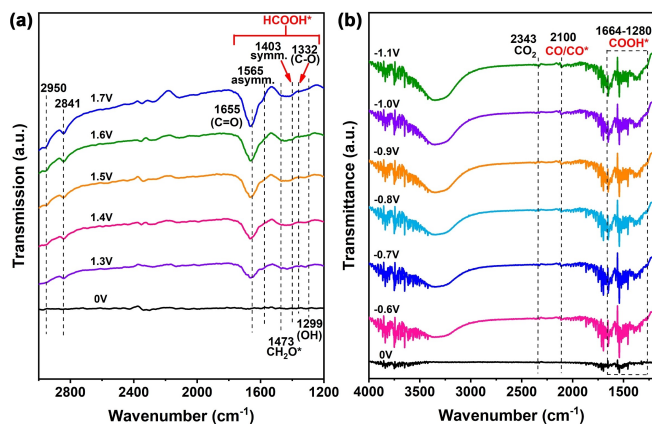


**Figure 4.** In situ FTIR spectra of PCN-601 for electrocatalysis: a) In situ FTIR spectra of PCN-601 for MOR. b) In situ FTIR spectra of PCN-601 for  $\text{CO}_2\text{RR}$ .

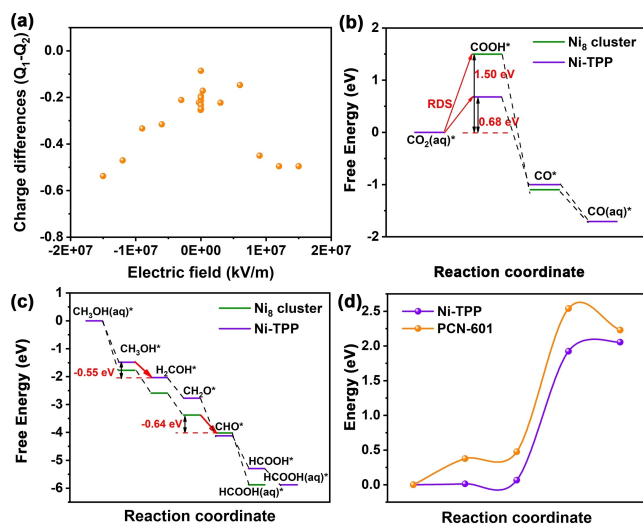


**Figure 5.** Density functional theory calculations: a) Difference between Ni charge from porphyrin ( $Q_1$ ) and  $\text{Ni}_8$  cluster ( $Q_2$ ). Since  $\text{Ni}_8$  cluster contains multi-Ni atoms,  $Q_2$  is taken the average values of them. Charges values are calculated by Bader charge analysis. b) Free energy diagram (FED) of  $\text{Ni}_8$  cluster and Ni-TPP for MOR. c) FED of  $\text{Ni}_8$  cluster and Ni-TPP for  $\text{CO}_2\text{RR}$ . The applied electrode potentials for (c) and (d) are 1.0 and  $-1.0$  V, respectively. d) Minimum energy path of the RDS ( $\text{CO}_2 + \text{H} + \text{e} \rightarrow \text{COOH}^*$ ) in the presence of pyrazole group or benzene ring.

groups. So, the NEB simulation of the RDS ( $\text{CO}_2 + \text{H} + \text{e} \rightarrow \text{COOH}^*$ ) is executed. We did two parallel NEB simulations, respectively with pyrazole and benzene being the  $\text{OH}^-$  acceptor. This  $\text{OH}^-$  is generated after the O–H bond of water cracks and the proton releases. Thus, the higher oxophilicity, stronger  $\text{OH}^-$  adsorption, and faster proton releases. Consequently, NEB simulations show the activation energy with the pyrazole group is significantly lower compared with the benzene ring (2.05 vs. 2.53 eV, Figure 5d). This proves that the pyrazole group can reduce the energy barrier. To sum up, as a catalyst, PCN-601 has two features in improving performance: 1) charge of  $\text{Ni}_8$  cluster can transfer to porphyrin under the electric field, resulting in improved MOR and  $\text{CO}_2\text{RR}$  performance; 2) PCN-601 can provide oxophilic pyrazole group to promote the proton migration reaction of  $\text{CO}_2\text{RR}$ .

## Conclusion

In summary, for the first time, we used a crystalline coordination catalyst (PCN-601) to realize the use of one catalyst as both anode and cathode for the hybrid electrocatalytic full reaction ( $\text{CO}_2\text{RR}$  coupled with MOR instead of OER). Moreover, due to the transference of electrons from electron-rich  $\text{Ni}_8$  clusters to the electron-deficient Ni ions in porphyrins, both anode and cathode show significantly high electrocatalytic activities and high Faradaic efficiencies for MOR (93.5%) and  $\text{CO}_2\text{RR}$  (94.5%). The performance can be further improved by light irradiation ( $\text{FE}_{\text{HCOOH}} > 90\%$  at all applied potentials and  $\text{FE}_{\text{CO}}$  nearly 100%). In addition to the high-value product ( $\text{HCOOH}$ ) at the anode rather than low-value  $\text{O}_2$ , the hybrid electrolyzer requires a low cell voltage of 1.99 V to achieve  $5 \text{ mA cm}^{-2}$  for the overall reaction, which is 310 mV lower than that of conventional overall  $\text{CO}_2\text{RR}$ . This work is the first report on the use of the same crystalline coordination compound as the catalyst to complete the catalytic reaction at both the anode and cathode of a hybrid electrocatalytic full reaction with very high Faraday efficiency. Besides, this work provides an important case study and a new design strategy to construct more crystalline electrocatalysts with high performance for hybrid  $\text{CO}_2$  electroreduction.

## Acknowledgements

This work was financially supported by the NSFC (Grants 92061101, 21871141, 21871142, 21901122, 22071109, 22105080, and 22101089); the Excellent Youth Foundation of Jiangsu Natural Science Foundation (No. BK20211593); Guangdong Basic and Applied Basic Research Foundation (No. 2020A1515110836); Science and Technology Planning Project of Guangzhou City (No. 202102020440); the Open Fund of Energy and Materials Chemistry Joint Laboratory of SCNU and TINCI (No. SCNU-TINCI-202204).

## Conflict of Interest

The authors declare no conflict of interest.

## Data Availability Statement

The data that support the findings of this study are available from the corresponding author upon reasonable request.

**Keywords:** Bifunctional Crystalline Catalysts · Crystalline Coordination Compounds · Hybrid  $\text{CO}_2$  Electroreduction · Methanol Oxidation

- [1] a) E. Huang Jianan, F. Li, A. Ozden, A. Sedighian Rasouli, F. P. García de Arquer, S. Liu, S. Zhang, M. Luo, X. Wang, Y. Lum, Y. Xu, K. Bertens, K. Miao Rui, C.-T. Dinh, D. Sinton, H. Sargent Edward, *Science* **2021**, 372, 1074–1078; b) J. Bednar, M. Obersteiner, A. Baklanov, M. Thomson, F. Wagner, O. Geden, M. Allen, J. W. Hall, *Nature* **2021**, 596, 377–383; c) S. Nitopi, E. Bertheussen, S. B. Scott, X. Liu, A. K. Engstfeld, S. Horch, B. Seger, I. E. L. Stephens, K. Chan, C. Hahn, J. K. Nørskov, T. F. Jaramillo, I. Chorkendorff, *Chem. Rev.* **2019**, 119, 7610–7672; d) R. Li, K. Xiang, Z. Peng, Y. Zou, S. Wang, *Adv. Energy Mater.* **2021**, 11, 2102292.
- [2] a) P. Ding, H. Zhao, T. Li, Y. Luo, G. Fan, G. Chen, S. Gao, X. Shi, S. Lu, X. Sun, *J. Mater. Chem. A* **2020**, 8, 21947–21960; b) M. B. Ross, P. De Luna, Y. Li, C.-T. Dinh, D. Kim, P. Yang, E. H. Sargent, *Nat. Catal.* **2019**, 2, 648–658; c) Z.-H. Zhu, B.-H. Zhao, S.-L. Hou, X.-L. Jiang, Z.-L. Liang, B. Zhang, B. Zhao, *Angew. Chem. Int. Ed.* **2021**, 60, 23394–23402; *Angew. Chem.* **2021**, 133, 23582–23590.
- [3] a) Y. Xu, B. Zhang, *ChemElectroChem* **2019**, 6, 3214–3226; b) C. Tang, R. Zhang, W. Lu, Z. Wang, D. Liu, S. Hao, G. Du, A. M. Asiri, X. Sun, *Angew. Chem. Int. Ed.* **2017**, 56, 842–846; *Angew. Chem.* **2017**, 129, 860–864; c) D. Wang, N. He, L. Xiao, F. Dong, W. Chen, Y. Zhou, C. Chen, S. Wang, *Angew. Chem. Int. Ed.* **2021**, 60, 24605–24611; *Angew. Chem.* **2021**, 133, 24810–24816.
- [4] X. Zhao, L. Du, B. You, Y. Sun, *Catal. Sci. Technol.* **2020**, 10, 2711–2720.
- [5] a) J. Na, B. Seo, J. Kim, C. W. Lee, H. Lee, Y. J. Hwang, B. K. Min, D. K. Lee, H.-S. Oh, U. Lee, *Nat. Commun.* **2019**, 10, 5193; b) L. Wang, Y. Zhu, Y. Wen, S. Li, C. Cui, F. Ni, Y. Liu, H. Lin, Y. Li, H. Peng, B. Zhang, *Angew. Chem. Int. Ed.* **2021**, 60, 10577–10582; *Angew. Chem.* **2021**, 133, 10671–10676; c) Y. Li, X. Wei, S. Han, L. Chen, J. Shi, *Angew. Chem. Int. Ed.* **2021**, 60, 21464–21472; *Angew. Chem.* **2021**, 133, 21634–21642; d) T. Wang, L. Tao, X. Zhu, C. Chen, W. Chen, S. Du, Y. Zhou, B. Zhou, D. Wang, C. Xie, P. Long, W. Li, Y. Wang, R. Chen, Y. Zou, X.-Z. Fu, Y. Li, X. Duan, S. Wang, *Nat. Catal.* **2022**, 5, 66–73; e) Y.-P. Wu, J.-W. Tian, S. Liu, B. Li, J. Zhao, L.-F. Ma, D.-S. Li, Y.-Q. Lan, X. Bu, *Angew. Chem. Int. Ed.* **2019**, 58, 12185–12189; *Angew. Chem.* **2019**, 131, 12313–12317.
- [6] C. Cao, D.-D. Ma, J. Jia, Q. Xu, X.-T. Wu, Q.-L. Zhu, *Adv. Mater.* **2021**, 33, 2008631.
- [7] a) X. Wei, Y. Li, L. Chen, J. Shi, *Angew. Chem. Int. Ed.* **2021**, 60, 3148–3155; *Angew. Chem.* **2021**, 133, 3185–3192; b) S. Sabatino, A. Galia, G. Saracco, O. Scialdone, *ChemElectroChem* **2017**, 4, 150–159; c) D. Wu, J. Hao, Z. Song, X.-Z. Fu, J.-L. Luo, *Chem. Eng. J.* **2021**, 412, 127893; d) Y. Huang, X. Chong, C. Liu, Y. Liang, B. Zhang, *Angew. Chem. Int. Ed.* **2018**, 57, 13163–13166; *Angew. Chem.* **2018**, 130, 13347–13350; e) M. S. E. Houache, R. Safari, U. O. Nwabara, T. Rafaideen,

- G. A. Botton, P. J. A. Kenis, S. Baranton, C. Coutanceau, E. A. Baranova, *ACS Appl. Energ. Mater.* **2020**, *3*, 8725–8738.
- [8] a) Q. Huang, Q. Li, J. Liu, Y. R. Wang, R. Wang, L. Z. Dong, Y. H. Xia, J. L. Wang, Y.-Q. Lan, *Matter* **2019**, *1*, 1656–1668; b) L. Zhang, X.-X. Li, Z.-L. Lang, Y. Liu, J. Liu, L. Yuan, W.-Y. Lu, Y.-S. Xia, L.-Z. Dong, D.-Q. Yuan, Y.-Q. Lan, *J. Am. Chem. Soc.* **2021**, *143*, 3808–3816; c) S. Li, Y. Gao, N. Li, L. Ge, X. Bu, P. Feng, *Energy Environ. Sci.* **2021**, *14*, 1897–1927.
- [9] a) Z.-B. Fang, T.-T. Liu, J. Liu, S. Jin, X.-P. Wu, X.-Q. Gong, K. Wang, Q. Yin, T.-F. Liu, R. Cao, H.-C. Zhou, *J. Am. Chem. Soc.* **2020**, *142*, 12515–12523; b) K. Wang, X.-L. Lv, D. Feng, J. Li, S. Chen, J. Sun, L. Song, Y. Xie, J.-R. Li, H.-C. Zhou, *J. Am. Chem. Soc.* **2016**, *138*, 914–919; c) N. Masciocchi, S. Galli, V. Colombo, A. Maspero, G. Palmisano, B. Seyyedi, C. Lamberti, S. Bordiga, *J. Am. Chem. Soc.* **2010**, *132*, 7902–7904.
- [10] S.-N. Sun, N. Li, J. Liu, W.-X. Ji, L.-Z. Dong, Y.-R. Wang, Y.-Q. Lan, *Natl. Sci. Rev.* **2021**, *8*, nwaal195.
- [11] a) W. Wang, Y. Wang, R. Yang, Q. Wen, Y. Liu, Z. Jiang, H. Li, T. Zhai, *Angew. Chem. Int. Ed.* **2020**, *59*, 16974–16981; *Angew. Chem.* **2020**, *132*, 17122–17129; b) W. Chen, C. Xie, Y. Wang, Y. Zou, C.-L. Dong, Y.-C. Huang, Z. Xiao, Z. Wei, S. Du, C. Chen, B. Zhou, J. Ma, S. Wang, *Chem* **2020**, *6*, 2974–2993; c) B. Zhou, Y. Li, Y. Zou, W. Chen, W. Zhou, M. Song, Y. Wu, Y. Lu, J. Liu, Y. Wang, S. Wang, *Angew. Chem. Int. Ed.* **2021**, *60*, 22908–22914; *Angew. Chem.* **2021**, *133*, 23090–23096.
- [12] Y. Zhao, J. Wang, R. Pei, *J. Am. Chem. Soc.* **2020**, *142*, 10331–10336.
- [13] Y. Lu, C.-L. Dong, Y.-C. Huang, Y. Zou, Z. Liu, Y. Liu, Y. Li, N. He, J. Shi, S. Wang, *Angew. Chem. Int. Ed.* **2020**, *59*, 19215–19221; *Angew. Chem.* **2020**, *132*, 19377–19383.
- [14] Q. Huang, J. Liu, L. Feng, Q. Wang, W. Guan, L.-Z. Dong, L. Zhang, L.-K. Yan, Y.-Q. Lan, H.-C. Zhou, *Natl. Sci. Rev.* **2020**, *7*, 53–63.
- [15] a) V. Kumaravel, J. Bartlett, S. C. Pillai, *ACS Energy Lett.* **2020**, *5*, 486–519; b) M. Lu, M. Zhang, C.-G. Liu, J. Liu, L.-J. Shang, M. Wang, J.-N. Chang, S.-L. Li, Y.-Q. Lan, *Angew. Chem. Int. Ed.* **2021**, *60*, 4864–4871; *Angew. Chem.* **2021**, *133*, 4914–4921.
- [16] J.-D. Yi, R. Xie, Z.-L. Xie, G.-L. Chai, T.-F. Liu, R.-P. Chen, Y.-B. Huang, R. Cao, *Angew. Chem. Int. Ed.* **2020**, *59*, 23641–23648; *Angew. Chem.* **2020**, *132*, 23849–23856.
- [17] a) N. J. Firet, W. A. Smith, *ACS Catal.* **2017**, *7*, 606–612; b) X. Wang, S. Xi, W. S. V. Lee, P. Huang, P. Cui, L. Zhao, W. Hao, X. Zhao, Z. Wang, H. Wu, H. Wang, C. Diao, A. Borgna, Y. Du, Z. G. Yu, S. Pennycook, J. Xue, *Nat. Commun.* **2020**, *11*, 4647; c) J. Li, R. Wei, X. Wang, Y. Zuo, X. Han, J. Arbiol, J. Llorca, Y. Yang, A. Cabot, C. Cui, *Angew. Chem. Int. Ed.* **2020**, *59*, 20826–20830; *Angew. Chem.* **2020**, *132*, 21012–21016.
- [18] a) S. Zhu, Q. Wang, X. Qin, M. Gu, R. Tao, B. P. Lee, L. Zhang, Y. Yao, T. Li, M. Shao, *Adv. Energy Mater.* **2018**, *8*, 1802238; b) S. Zhu, B. Jiang, W.-B. Cai, M. Shao, *J. Am. Chem. Soc.* **2017**, *139*, 15664–15667.
- [19] J. K. Nørskov, J. Rossmeisl, A. Logadottir, L. Lindqvist, J. R. Kitchin, T. Bligaard, H. Jónsson, *J. Phys. Chem. B* **2004**, *108*, 17886–17892.
- [20] J. Hao, J. Liu, D. Wu, M. Chen, Y. Liang, Q. Wang, L. Wang, X.-Z. Fu, J.-L. Luo, *Appl. Catal. B* **2021**, *281*, 119510.
- [21] a) J. A. Gauthier, S. Ringe, C. F. Dickens, A. J. Garza, A. T. Bell, M. Head-Gordon, J. K. Nørskov, K. Chan, *ACS Catal.* **2019**, *9*, 920–931; b) J. A. Gauthier, C. F. Dickens, H. H. Heenen, S. Vijay, S. Ringe, K. Chan, *J. Chem. Theory Comput.* **2019**, *15*, 6895–6906; c) G. Wang, J. Chen, K. Li, J. Huang, Y. Huang, Y. Liu, X. Hu, B. Zhao, L. Yi, T. W. Jones, Z. Wen, *Nano Energy* **2022**, *92*, 106751.
- [22] a) D. Strmcnik, M. Uchimura, C. Wang, R. Subbaraman, N. Danilovic, D. van der Vliet, A. P. Paulikas, V. R. Stamenkovic, N. M. Markovic, *Nat. Chem.* **2013**, *5*, 300–306; b) D. Strmcnik, P. P. Lopes, B. Genorio, V. R. Stamenkovic, N. M. Markovic, *Nano Energy* **2016**, *29*, 29–36.

Manuscript received: May 20, 2022

Accepted manuscript online: June 24, 2022

Version of record online: July 13, 2022